

The Anderson–Holstein Model in Two Flavors of the Non–Crossing Approximation

Hsing-Ta Chen,¹ Guy Cohen,^{1,2} Andrew J. Millis,² and David R. Reichman¹

¹*Department of Chemistry, Columbia University, New York, New York 10027, U.S.A.*

²*Department of Physics, Columbia University, New York, New York 10027, U.S.A.*

The dynamical interplay between electron–electron interactions and electron–phonon coupling is investigated within the Anderson–Holstein model, a minimal model for open quantum systems that embody these effects. The influence of phonons on spectral and transport properties is explored in equilibrium, for non-equilibrium steady state and for transient dynamics after a quench. Both the particle–hole symmetric and the more generic particle–hole asymmetric cases are studied. The treatment is based on two complementary non-crossing approximations, the first of which is constructed around the weak-coupling limit and the second around the polaron limit. In general, the two methods disagree in nontrivial ways, indicating that more reliable approaches to the problem are needed. The frameworks used here can form the starting point for numerically exact methods based on bold-line continuous-time quantum Monte Carlo algorithms capable of treating open systems simultaneously coupled to multiple fermionic and bosonic baths.

I. INTRODUCTION

The interaction between electrons and phonons plays an essential role in condensed matter physics: it is for example the fundamental factor responsible for the resistivity of conduction electrons in crystals at relatively high temperatures and the onset of superconductivity at low temperatures.¹ In non-equilibrium molecular electronics experiments,^{2–4} electron–phonon interactions are ever present and have major implications^{5,6} which can be exploited in the design of phononic devices.^{7,8} In addition, the interplay between electron–electron interactions (responsible for Coulomb blockade and the Kondo effect) and electron–phonon scattering leads to novel and subtle behaviors.^{9,10} For example, conductance side peaks replicating the Kondo resonance^{9,11,12} and negative differential resistance at voltages corresponding to the vibrational energy of the molecule¹³ have been observed. In a broader sense, explicating the role played by electron–phonon interactions in strongly correlated materials remains a fertile area of research, where recent interest has focused, for example, on the role played by phonons in fulleride,¹⁴ cuprate¹⁵ and pnictide superconductors^{16,17} and the control of superconductivity and metal–insulator transitions in correlated materials via strong laser fields.^{18–22}

A standard model that simultaneously describes both electronic interactions and electron–phonon coupling in nanoscale devices is the Anderson–Holstein model.^{23–25} This model consists of a single interacting site (sometimes called the dot or impurity) coupled to a non-interacting electron reservoir (or reservoirs) and to a set of localized phonon modes. The Anderson–Holstein model can be considered a minimal description of the essential aspects of a correlated electron system interacting with phonon excitations, and has been used to describe vibrational effects in molecular electronics.^{25–28} Furthermore, within the framework of dynamical mean-field theory (DMFT),²⁹ the characterization of a strongly correlated

material with active phonon degrees of freedom may be effectively reduced to the Anderson–Holstein model and its variants.^{27,30,31}

Despite the importance of the Anderson–Holstein model, there is surprisingly little known about its real-time dynamical properties outside of simple limits where perturbation arguments can be made. The case of zero on-site electron–electron interactions can describe some phenomena associated with the electron–phonon interaction, including non-equilibrium transient dynamics, inelastic transport, and phonon-induced side peaks.^{32–36} This limit has been widely considered in the literature; despite its simplicity, it is non-trivial to solve, especially out of equilibrium. A variety of techniques have been used to analyze this model, including perturbation theory in the electron–phonon coupling,³⁷ a semi-classical treatment,³⁸ and master-equation approaches.^{37,39–43} Semi-analytical approximations within nonequilibrium Keldysh Green’s functions (NEGF),^{44–50} the equation-of-motion (EOM) approach,^{51–54} an interpolative ansatz,⁵⁵ and a recent dressed tunneling approximation³⁴ have been applied to the model in various limits. Numerically exact methods have also been applied, including real-time Quantum Monte Carlo (QMC),^{35,36,56,57} iterative path integral schemes^{58–60} and the multi-layer multi-configuration time-dependent Hartree (ML-MCTDH) method.^{61,62}

Treatment of the combined effect of electron–electron and electron–phonon interactions is simplest when the on-site Coulomb repulsion is effectively infinite ($U \rightarrow \infty$). In this limit, some methods used to treat the non-interacting case can be adopted and generalized, including certain Monte Carlo approaches,^{28,63} the equation-of-motion technique,^{64–67} a decoupling scheme for NEGF,⁶⁸ and the slave-boson technique^{69,70}. Studies of the infinite- U Anderson–Holstein model predict non-trivial effects, such as the appearance of Kondo replicas above and below the chemical potential and negative differential resistance associated with the destruction of the Kondo resonance.^{13,28} However it remains unclear if these predictions are valid outside of linear response from equilib-

rium, and in general neither the $U = 0$ nor $U \rightarrow \infty$ limits describe the bulk of interesting cases of experimental relevance.

Only a handful of approaches are capable of calculating properties of a generic Anderson–Holstein model outside of the idealized limits discussed above. Approximate methods, such as the master equation approach, can accurately describe transport phenomena at high temperatures and large voltages.⁷¹ The ML-MCTDH method is numerically exact, but has difficulty converging for strong electron–phonon coupling or far from equilibrium.^{72,73} The numerical renormalization group (NRG) can also be extended to include electron–phonon interactions, but remains difficult to apply out of equilibrium and is generally reliable only for the low energy properties of the system.^{25,26,32,74–77} The auxiliary-field QMC method has been used to calculate the density of states under the influence of the phonons in imaginary time,⁷⁸ but application to dynamics involves an uncontrolled analytical continuation which is problematic at certain parameters,⁷⁹ and the Matsubara formulation is only valid for equilibrium and linear response properties. Real time QMC provides an alternative numerically exact approach which has the ability to describe transient dynamics and non-equilibrium transport properties over a wide range of parameters.^{30,56,80–82} In combination with reduced dynamics techniques^{83,84} it can sometimes be used to obtain results over very long timescales.⁸⁵ However, real time QMC is generically plagued by a dynamical sign problem which limits the accessible timescales. Although not the direct focus of this manuscript, we note that the approaches described here can provide a foundation to allow for an amelioration of the sign problem in QMC simulations.^{79,86}

The self-consistent resummation of particular classes of interaction terms may allow for an extension of the domain of validity provided by bare perturbation theory. A prominent example is provided by the non-crossing approximation (NCA).^{87,88} The NCA is a semi-analytical method based on the resummation to all orders of a specific subset of diagrams (those that do not cross temporally on the Keldysh contour) associated with the hybridization between the impurity and the non-interacting leads. It provides a computationally inexpensive approach for solving generic impurity models out of equilibrium.⁸⁹ NCA is exact in the atomic limit, and works best in the limit of infinite U and finite ϵ . The approximation does not fully capture low energy properties and does not correctly reproduce the noninteracting limit. But despite the quantitative inaccuracies, the NCA qualitatively predicts the emergence and some properties of the Kondo resonance, and is generally accurate for high-energy features. While the NCA as a "stand alone" approximation may quantitatively fail, higher order approximations (e.g. one-crossing approximation) based on the same principles have been used,^{90,91} and recent numerically exact QMC approaches have been formulated that sample corrections to the NCA in a numerically ex-

act way.^{79,86,92–94}

The NCA has been extended to include the electron–phonon coupling, via the slave-boson technique,^{69,70} in nonequilibrium DMFT studies,^{30,31} and within a pseudoparticle picture.⁹⁵ A first goal of our work is to clearly formulate two complementary NCA-like approximations in the full many-body basis of the impurity, in a form suitable for studying the non-equilibrium behavior of the Anderson–Holstein model, and to compare and contrast the predictions of these distinct self-consistent procedures. A second goal is to clearly delineate the diagrammatic rules associated with each self-consistent resummation on the Keldysh contour so that future exact QMC schemes which sample remaining diagrams may be explicitly formulated. The outline of this paper is as follows. In Sec. II we introduce the Anderson–Holstein model and provide the needed formalism. In Sec. III, two distinct types of NCA-like approximation are described. In Sec. IV, we present and compare results for transient dynamics, steady state spectral function and differential conductance for a generic Anderson–Holstein model in the Kondo regime. A summary and conclusion are presented in Sec. V.

II. COUPLING EXPANSION FOR ANDERSON–HOLSTEIN MODEL

A. Model and definitions

We consider a single spin-degenerate impurity or quantum dot level with a linear coupling to a phonon bath and to a pair of metallic leads which will be referred to as “left” (L) and “right” (R). This model is described by the nonequilibrium Anderson–Holstein Hamiltonian^{25–27}

$$H = H_d + H_b + V_b + \sum_{\ell \in L, R} (H_\ell + V_\ell). \quad (1)$$

The electronic part of the dot Hamiltonian, H_d , is

$$H_d = \sum_{\sigma=\uparrow, \downarrow} \epsilon_\sigma n_\sigma + U n_\uparrow n_\downarrow, \quad (2)$$

where ϵ_σ denotes the energy of singly-occupied states and U is the Coulomb interaction. The operators d_σ^\dagger creates an electron of spin σ on the dot and the occupation $n_\sigma = d_\sigma^\dagger d_\sigma$.

The local phonon bath Hamiltonian is

$$H_b = \sum_q \omega_q b_q^\dagger b_q. \quad (3)$$

Here the b_q^\dagger are phonon creation operators, and ω_q is the frequency associated with a phonon mode q . We will typically assume that the phonons are initially in equilibrium, such that the occupation of the phonon modes is given by the Bose–Einstein distribution $\langle b_q^\dagger b_q \rangle = \frac{1}{e^{\beta_d \omega_q} - 1}$, β_d

being the inverse temperature of the phonon bath. The electron-phonon coupling Hamiltonian V_b is

$$V_b = \sum_q \lambda_q (b_q^\dagger + b_q) (n_d - \delta), \quad (4)$$

where $n_d = \sum_\sigma n_\sigma$ is the total electronic occupation of the dot and λ_q the coupling strength between the dot and phonon mode q . The parameter δ is of no physical significance, in the sense that it may be absorbed into a redefinition of the zero point of the oscillator coordinate. However, it is convenient to set $\delta = 1$, so that $\epsilon = 0$ describes the particle-hole symmetric dot, and we will primarily consider this case. We will also investigate the case $\delta = 0$, which provide a more convenient description of a molecular junction in which polaron formation is linked to the presence of extra electrons on the dot. In either case, the electron-phonon coupling is characterized by a spectral density $J(\omega) \equiv \frac{\pi}{2} \sum_q \frac{\lambda_q^2}{\omega_q} \delta(\omega - \omega_q)$.

The left and right lead Hamiltonians are

$$H_\ell = \sum_{k \in \ell} \sum_\sigma \epsilon_k c_{k\sigma}^\dagger c_{k\sigma}, \quad (5)$$

with $\ell \in \{L, R\}$ and the index k denoting a level within a lead. We assume the leads to be non-interacting, such that they are fully described by the dispersion relation ϵ_k and the creation operators $c_{k\sigma}^\dagger$. The leads are taken to each be initially isolated and at an equilibrium state with density matrix ρ_ℓ , and their thermodynamic properties characterized by an inverse temperature β_ℓ and a chemical potential μ_ℓ . The initial density of states is then described by a Fermi-Dirac distribution, $\langle c_{k\sigma}^\dagger c_{k\sigma} \rangle = f_\ell(\epsilon_k) = \frac{1}{e^{\beta_\ell(\epsilon_k - \mu_\ell)} + 1}$. The hybridization V_ℓ between the dot and lead electrons is described by the dot-lead coupling Hamiltonian

$$V_\ell = \sum_{k \in \ell} \sum_\sigma \left[t_k d_\sigma c_{k\sigma}^\dagger + t_k^* d_\sigma^\dagger c_{k\sigma} \right], \quad (6)$$

where t_k enumerates the coupling strength between the dot and level k of lead ℓ . We define a coupling density $\Gamma_\ell(\omega) = 2\pi \sum_{k \in \ell} |t_k|^2 \delta(\omega - \epsilon_k)$, which fully characterizes the t_k within this model.

In steady state the dynamical response of a system is characterized by its spectral function

$$A(\omega) = \frac{i}{2\pi} \text{Tr} \{ G^r(\omega) - G^a(\omega) \}, \quad (7)$$

which may be considered a probe of the density of electron and hole excitations as a function of energy. To calculate the spectral function at frequency ω' , we use the auxiliary current method^{79,93} by appending two auxiliary leads to the model, $H \rightarrow H + H_A + V_A$, where $H_A = \sum_{k \in A} \epsilon_k a_k^\dagger a_k$ and $V_A = \sum_{k \in A} \sum_\sigma \left[t_k d_\sigma a_k^\dagger + t_k^* d_\sigma^\dagger a_k \right]$. These auxiliary leads are coupled to the dot at the single frequency ω' with a spectral density $\Gamma_A'(\omega) = \eta \delta(\omega - \omega')$.

One lead is kept fully occupied, such that $f_{A1}(\omega) = 1$; the other lead is kept empty, such that $f_{A0}(\omega) = 0$. We can calculate the *auxiliary* spectral function $A(\omega; t)$ at any finite time by the following relation:

$$A(\omega; t) = \lim_{\eta \rightarrow 0} -\frac{2\hbar}{e\pi\eta} [I_{A1}^\omega(t) - I_{A0}^\omega(t)]. \quad (8)$$

Here, $I_{A0}^\omega(t)$ and $I_{A1}^\omega(t)$ are the currents flowing out of lead A0 and A1, respectively, at time t . At long times, the auxiliary spectral function approaches the steady state spectral function, Eq. 7. While at finite times the auxiliary spectral function does not conform to the standard definition of a spectral function in terms of a Fourier transform of a correlation function, it retains the appealing physical interpretation as a measure of the single-particle excitation density in energies, and could in principle be accessed experimentally by way of three-lead experiments.^{79,93,96,97}

We shall also be interested in the differential conductance,

$$G(V) = \frac{d}{dV} (I_L - I_R). \quad (9)$$

which is directly accessible in transport experiments. Here, $V = \mu_L - \mu_R$ is the bias voltage between the two leads. The current $I_\ell(t)$ out of lead ℓ is given by $I_\ell(t) = \langle \mathcal{I}_\ell(t) \rangle$, where the current operator for a given lead,

$$\mathcal{I}_\ell = \dot{N}_\ell = i \sum_{k \in \ell} \left(t_k c_{k\sigma}^\dagger d_\sigma - t_k^* c_{k\sigma} d_\sigma^\dagger \right), \quad (10)$$

describes the rate at which carriers flow out of that lead. The differential conductance is often interpreted as an estimator for the equilibrium spectral function of the model. However, this interpretation is only valid if the spectral function is independent of the bias voltage. In practice, the two quantities may be qualitatively different.⁹³

B. Coupling expansion: general formalism

We now formulate a double expansion in the electron-phonon and dot-lead couplings. A brief review will be provided here for completeness; we refer readers interested in a more detailed technical outline of the formalism and algorithm elsewhere.⁷⁹ We begin by recasting the Hamiltonian as $H = H_0 + V$. H_0 describes the isolated dot and bath subsystems, while $V = V_b + \sum_\ell V_\ell$ describes the coupling Hamiltonian.

The expectation value of an operator \mathcal{O} at time t can be written in the form $\langle \mathcal{O}(t) \rangle = \langle e^{iHt} \mathcal{O} e^{-iHt} \rangle = \langle U^\dagger(t) \mathcal{O}_I(t) U(t) \rangle$, where $U(t) = e^{iH_0 t} e^{-iH t}$ and $\mathcal{O}_I(t) = e^{iH_0 t} \mathcal{O} e^{-iH_0 t}$. The subscript I denotes an operator in the interaction picture. We also define thermal averaging by way of the notation $\langle \mathcal{O} \rangle \equiv \text{Tr} \{ \rho \mathcal{O} \}$, with the averaging

performed with respect to the uncorrelated initial density matrix formed by the product of subsystem density matrices: $\rho = \rho_d \otimes \prod_\ell \rho_\ell \otimes \rho_b$. Thus the dynamics that appear in the following are not in equilibrium and illustrate the approach to equilibrium in the appropriate limits. Other than in some very special cases, a *finite* system coupled to an infinite thermal bath which is allowed to evolve in time is generally found to reproduce the steady state results at long times. Moreover, this is often the only rigorous way to construct the correct nonequilibrium steady state in open quantum systems. Initial correlations allow the system to be thermalized at time zero. Within DMFT,^{27,30,31,91,98} one deals with an *infinite* interacting system which is not coupled to a bath, and the role of the initial correlations therefore becomes more important. They are needed to model an initially thermalized system, which might be thought of as a system that had been weakly coupled to a bath and allowed to relax before the beginning of the calculation.

We now describe the details of a Dyson expansion for the reduced propagator on the Keldysh contour. We can expand $U(t)$ in a Dyson series

$$U(t) = \sum_{n=0}^{\infty} (-i)^n \int_0^t dt_1 \int_0^{t_1} dt_2 \cdots \int_0^{t_{n-1}} dt_n \quad (11)$$

$$\times V_I(t_1) V_I(t_2) \cdots V_I(t_n),$$

such that the propagator can be expressed as $e^{-iHt} = e^{-iH_0 t} U(t)$. We adopt the many-body atomic states of the isolated dot, $\{|\alpha\rangle\} = \{|00\rangle \equiv |0\rangle, |\uparrow\rangle \equiv |1\rangle, |\downarrow\rangle \equiv |2\rangle, |\uparrow\downarrow\rangle \equiv |3\rangle\}$, as a basis, and define the reduced propagator matrix element $G_{\alpha\beta}(t) \equiv \langle \alpha | \text{Tr}_B \{ \rho e^{-iHt} \} | \beta \rangle$. The trace is taken over the lead and phonon degrees of freedom: $\text{Tr}_B \equiv \text{Tr}_\ell \text{Tr}_b$. The remaining quantity is reduced to the dimensionality of the (many-body) dot subspace. We also define the unperturbed reduced propagator $G_{\alpha\beta}^{(0)}(t) \equiv \langle \alpha | \text{Tr}_B \{ \rho e^{-iH_0 t} \} | \beta \rangle$. $G_{\alpha\beta}^{(0)}$ is diagonal for the model treated here, and takes the form $G_{\alpha\beta}^{(0)}(t) = \Phi(t) \delta_{\alpha\beta} e^{-iE_\alpha t}$. The state energy E_α is evaluated from the isolated dot Hamiltonian. The factor $\Phi(t) = \text{Tr}_B \{ \rho e^{-i(H_0 - H_d)t} \}$ is related to fluctuations in the noninteracting baths, and is independent of the dot state. It is exactly canceled when considering any quantity defined on the two branch Keldysh contour, and can therefore be safely ignored.

The full, or perturbed, reduced propagator $G_{\alpha\beta}(t)$ is also diagonal. Contributions to it from the coupling Hamiltonian are nonzero only when the creation and annihilation operators occur in pairs, such that only even orders must be accounted for:

$$G_{\alpha\alpha}(t) = G_{\alpha\alpha}^{(0)}(t) - \int_0^t dt_1 \int_0^{t_1} dt_2 \quad (12)$$

$$\times \langle \alpha | \text{Tr}_B \{ \rho e^{-iH_0 t} V_I(t_1) V_I(t_2) \} | \alpha \rangle$$

$$+ \cdots$$

This series can be represented as a summation of diagrams in which the coupling Hamiltonian appears an even number of times. An example diagram is shown Fig. 1: in (a), the representation of $G_{\alpha\alpha}^{(0)}$ (thin lines) and $G_{\alpha\alpha}$ (bold lines) in terms of pairs of solid and dashed lines is shown. In (b) a diagram is shown which contains Fermion hybridizations, denoted by wiggly lines which change the dot population, and phonon interactions, denoted by wavy lines with loops which do not change the population (and may appear only within certain dot states, as detailed below).

The reduced propagator satisfies a causal Dyson equation of the form

$$G_{\alpha\alpha}(t) = G_{\alpha\alpha}^{(0)}(t) + \int_0^t dt_1 \int_0^{t_1} dt_2 \quad (13)$$

$$\times G_{\alpha\alpha}^{(0)}(t - t_1) \Sigma_{\alpha\alpha}(t_1, t_2) G_{\alpha\alpha}(t_2),$$

where all non-trivial aspects of the problem are contained in the (proper) self energy $\Sigma_{\alpha\alpha}(t_1, t_2)$. Solving the Dyson equation self-consistently is in itself an inexpensive computation if the self energy is known. Within the hybridization expansion for the phonon-free version of the model, the simplest approximation to the self energy includes only a single pair of coupling Hamiltonians:

$$\Sigma_{\alpha\alpha}^{2\text{BA}}(t_1 - t_2) = -\langle \alpha | \text{Tr}_b \{ \rho V e^{-iH_0(t_1 - t_2)} V \} | \alpha \rangle \quad (14)$$

$$= \sum_{\beta} G_{\beta\beta}^{(0)}(t_1 - t_2) \times \Delta_{\alpha\alpha}^{\beta}(t_1 - t_2),$$

where the hybridization function is defined as

$$\Delta_{\alpha\alpha}^{\beta}(t_1 - t_2) \equiv -\langle \alpha | \text{Tr}_b \{ \rho V_I(t_1) | \beta \rangle \langle \beta | V_I(t_2) \} | \alpha \rangle. \quad (15)$$

This is known as the second-order Born approximation (2BA). The non-crossing approximation (NCA), also known as the self-consistent Born approximation (SCBA), takes the same form, but inserts the full propagator G into the self energy:

$$\Sigma_{\alpha\alpha}^{\text{NCA}}(t_1 - t_2) = \sum_{\beta} G_{\beta\beta}(t_1 - t_2) \times \Delta_{\alpha\alpha}^{\beta}(t_1 - t_2). \quad (16)$$

With this self energy, we can obtain an approximate propagator containing an infinite, but partial, subset of the diagrams contributing to the reduced propagator, namely all diagrams in which hybridization lines do not cross each other. In the following section, two ways of generalizing this idea to the full Anderson-Holstein model will be described.

So far, in order to simplify the discussion, we have limited our attention to a reduced propagator living on a single branch of the Keldysh contour. To calculate a physical observable, we must consider a two-branch Keldysh contour with the observable operator \mathcal{O} placed at the final time t , and take into account diagrams with lines crossing between the two branches. To this end, we define a vertex function of the observable \mathcal{O} , with the two

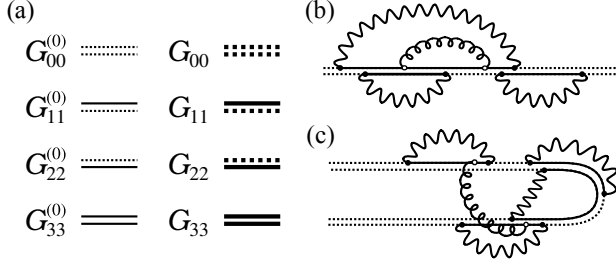


Figure 1. (a) The elements of the unperturbed propagator $G_{\alpha\alpha}^{(0)}$ (left column, thin lines) and of the NCA propagator $G_{\alpha\alpha}$ (right column, bold lines). The upper line represents spin up occupation and the lower line spin down occupation. The dotted line signifies that the spin level is unoccupied, while a solid line marks it as occupied. (b) An example of a diagram included in the reduced propagator G_{00} . Electronic hybridization lines are shown as wiggly lines, and phonon interaction lines as gluon lines. (c) An example of a diagram on the Keldysh contour with inter-branch lines and a special hybridization line ending at the final time, corresponding to a contribution to the current.

time variables t and t' placed on opposite branches of the contour. With $t' \rightarrow t$, this object yields the physical expectation value of observable $\mathcal{O}(t)$. In particular, the current out of the lead ℓ can be obtained from $I_\ell(t) = \langle \mathcal{I}_\ell(t) \rangle$, where the current operator

$$\mathcal{I}_\ell = \dot{N}_\ell = i \sum_{k \in \ell} \left(t_k c_{k\sigma}^\dagger d_\sigma - t_k^* c_{k\sigma} d_\sigma^\dagger \right) \quad (17)$$

and the c and d operators are understood to be at the tip of the Keldysh contour.

Because \mathcal{I}_ℓ is composed of the same operators appearing in the dot-bath hybridization Hamiltonian, within the coupling expansion the current can be obtained by summing over diagrams which have a special hybridization line placing the current operator at the final time of the Keldysh contour. An example of such a diagram is given in Fig. 1 (c).

III. TWO TYPES OF NCA FOR ELECTRON-PHONON COUPLING

In this section we lay out the construction of NCA-like approximations in two limits: First, a *bare NCA* based on self-consistently resummed *second order* perturbation theory for the electron-phonon and dot-lead and electron-phonon Hamiltonians. Second, a *dressed NCA* in which the Hamiltonian is modified by a Lang-Firsov transformation so that the coupling Hamiltonian becomes a phonon-dressed dot-lead coupling, and includes non-crossing diagrams composed of phonon-dressed hybridization lines.^{27,30} Both approximations can be extended to higher orders, or used as the preliminary step

withing a numerically exact bold-line QMC algorithm. We initially formulate these two types of NCA for the symmetric Anderson-Holstein model in the following two subsections, then discuss the asymmetric case.

A. Weak coupling perturbation theory

The *bare NCA* approximation is specified by the following equations

$$\mathbf{G}^{-1} = \mathbf{G}_0^{-1} - \Sigma^\ell - \Sigma^b, \quad (18)$$

with \mathbf{G} , \mathbf{G}_0 and Σ matrices (diagonal, in the cases of interest here) in the Hilbert space of the decoupled dot, and the lead (ℓ) and phonon (b) self energies Σ given by

$$\Sigma_{\alpha\alpha}^\ell(t_1, t_2) = \sum_{\beta} G_{\beta\beta}(t_1, t_2) \times \Delta_{\alpha\alpha}^\beta(t_1, t_2) \quad (19)$$

$$\Sigma_{\alpha\alpha}^b(t_1, t_2) = G_{\alpha\alpha}(t_1, t_2) \times \Lambda_{\alpha\alpha}(t_1, t_2) \quad (20)$$

with the lead hybridization function

$$\begin{aligned} \Delta_{\alpha\alpha}^\beta(t_1, t_2) = & \sum_{\sigma} \langle \alpha | d_\sigma | \beta \rangle \langle \beta | d_\sigma^\dagger | \alpha \rangle \sum_{k \in \ell} |t_k|^2 \text{Tr}_\ell \left[\rho_\ell c_{k\sigma}^\dagger(t_1) c_{k\sigma}(t_2) \right] \\ & + \sum_{\sigma} \langle \alpha | d_\sigma^\dagger | \beta \rangle \langle \beta | d_\sigma | \alpha \rangle \sum_{k \in \ell} |t_k|^2 \text{Tr}_\ell \left[\rho_\ell c_{k\sigma}(t_1) c_{k\sigma}^\dagger(t_2) \right]. \end{aligned} \quad (21)$$

We also define the lesser and greater hybridization functions $\Delta_\ell^{<,>}(\tau_1, \tau_2) = \sum_{k \in \ell} |t_k|^2 \text{Tr}_\ell \left[\rho c_{k\sigma}^\dagger(\tau_1) c_{k\sigma}(\tau_2) \right]$ for each lead ℓ and times τ_1, τ_2 on the Keldysh contour. $\Delta_\ell^>$ is used when τ_1 precedes τ_2 , and $\Delta_\ell^{<}$ is used otherwise. The dot-lead hybridization function for each lead can be expressed in terms of the coupling densities $\Gamma_\ell(\omega)$ and the initial occupation of that lead:

$$\Delta_\ell^>(t_1, t_2) = i \int_{-\infty}^{\infty} \frac{d\omega}{\pi} e^{-i\omega(t_1-t_2)} \Gamma_\ell(\omega) [1 - f_\ell(\omega - \mu_\ell)], \quad (22)$$

$$\Delta_\ell^{<}(t_1, t_2) = -i \int_{-\infty}^{\infty} \frac{d\omega}{\pi} e^{-i\omega(t_1-t_2)} \Gamma_\ell(\omega) f_\ell(\omega - \mu_\ell). \quad (23)$$

We similarly define the phonon hybridization function

$$\begin{aligned} \Lambda_{\alpha\alpha}(t_1, t_2) = & \langle \alpha | (n_d(t_1) - \delta) (n_d(t_2) - \delta) | \alpha \rangle \times \\ & \sum_q \lambda_q^2 \text{Tr}_b \left[\rho_b (b_q^\dagger(t_1) + b_q(t_1)) (b_q^\dagger(t_2) + b_q(t_2)) \right]. \end{aligned} \quad (24)$$

This is analogous (but not identical) to the pseu-

doparticle NCA approximation of ref. 95. Since the the electron-phonon coupling V_b does not modify the electronic state of the dot, one can write $\langle \alpha | (n_d(t_1) - \delta) (n_d(t_2) - \delta) | \alpha \rangle = \left(n_d^{(\alpha)} - \delta \right)^2$. We also define the bath correlation function, $B_q(t_1, t_2) = \text{Tr}_b [\rho_b (b_q^\dagger(t_1) + b_q(t_1)) (b_q^\dagger(t_2) + b_q(t_2))]$. It can be expressed in terms of the frequency ω_q and the inverse temperature β of the local phonon modes, $B_q(t) = \coth(\beta\omega_q/2) \cos(\omega_q t) - i \sin(\omega_q t)$, if we consider a bath initially composed of free harmonic phonon modes. Thus, it is possible to recast the phonon hybridization function as $\Lambda_{\alpha\alpha}(t_1 - t_2) = \left(n_d^{(\alpha)} - \delta \right)^2 \times \Lambda_b(t_1 - t_2)$, where

$$\Lambda_b(t_1 - t_2) = \sum_q \lambda_q^2 B_q(t_1 - t_2). \quad (25)$$

Just as the electronic hybridization function is described by $\Gamma_\ell(\omega)$, the phonon bath is usually characterized by its spectral density, $J(\omega) = \frac{\pi}{2} \sum_q (\lambda_q^2/\omega_q) \delta(\omega - \omega_q)$. In particular,

$$\Lambda_b(t_1 - t_2) = \frac{2}{\pi} \int d\omega J(\omega) \omega B_\omega(t_1 - t_2). \quad (26)$$

Fig. 2 and Fig. 3 illustrate the diagrams included in the self energy of the *bare NCA* approach (for the symmetric case $\delta = 1$). The wiggly lines in Fig. 2 denote the dot-lead hybridization $\Delta_{\alpha\alpha}^\beta(t_1 - t_2)$, while the phonon lines of Fig. 3 symbolize the phonon coupling $\Lambda_{\alpha\alpha}(t_1 - t_2)$. The computation of the Green's function from the Dyson equation using this approximate self energy embodies a self-consistent perturbative expansion including the lowest order skeleton diagrams in both the dot-lead hybridization and electron-phonon coupling. We expect this bare NCA approach to be more applicable in the regime where both λ and Γ are small. Additionally, the Green's function resulting from the bare NCA does not contain certain multi-phonon excitations, related to crossing diagrams, which might be expected to affect the dot electron if the phonon relaxation is slow. This implies that the bare NCA is more accurate in the limit of the fast phonon bath.

B. Strong coupling perturbation theory

In this section, we present a version of the non-crossing approximation more suitable to strong coupling between the dot and the phonon bath to the propagator formulation. This approach, which we will refer to as the *dressed NCA*, has previously been employed within a standard Green's function formulation in ref. 27 and 30.

We begin by performing the unitary Lang-Firsov transformation $\tilde{H} = SHS^{-1}$ with $S = e^{\frac{\lambda}{\omega_0}(b^\dagger - b)n_d}$, which eliminates the explicit electron-phonon coupling in the Hamiltonian. We set the unperturbed Hamiltonian to

Figure 2. The electron hybridization diagrams included in the bare NCA self energy, where the wiggly lines denote electronic dot-lead hybridization lines. The pairs of straight lines represent the dot's electronic state, with the two lines standing for the two possible spins: a solid line represents an occupied spin level, whereas dashed lines stand for empty spin levels.

Figure 3. The phonon interaction diagrams for the bare NCA self energy in the symmetric case $\delta = 1$. The curly lines denote phonon interaction lines, and straight lines are as in Fig. 2.

be $H_0 = H_d + H_b + V_b$. After the transformation, this becomes

$$\tilde{H}_0 = \tilde{\epsilon}_d \tilde{n}_d + \tilde{U} \tilde{n}_\uparrow \tilde{n}_\downarrow, \quad (27)$$

$$\tilde{V}_\ell = \sum_{k \in \ell} \sum_{\sigma} \left[t_k \tilde{d}_\sigma c_{k\sigma}^\dagger + t_k^* \tilde{d}_\sigma^\dagger c_{k\sigma} \right]. \quad (28)$$

In the above expressions, the bare dot energy ϵ and the Coulomb interaction strength U are replaced by the renormalized quantities

$$\tilde{\epsilon} = \epsilon + (2\delta - 1)\lambda^2/\omega_0, \quad (29)$$

$$\tilde{U} = U - 2\lambda^2/\omega_0. \quad (30)$$

Also, the dot electron creation and annihilation operators become

$$\tilde{d}_\sigma = e^{-\frac{\lambda}{\omega_0}(b^\dagger - b)} d_\sigma, \quad (31)$$

$$\tilde{d}_\sigma^\dagger = e^{\frac{\lambda}{\omega_0}(b^\dagger - b)} d_\sigma^\dagger. \quad (32)$$

All pairs of hybridization events are therefore connected

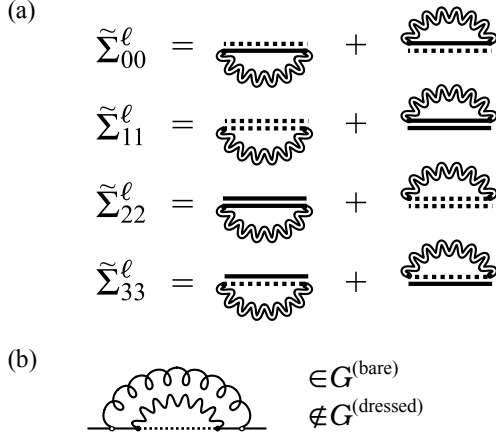


Figure 4. (a) The diagrams representing the different matrix elements of the dressed NCA self energy. The wiggly double lines denote electron hybridization lines dressed by phonon interactions. (b) An example of a bare NCA diagram of the lowest order is not included in the dressed NCA diagrams.

by an infinite set of phonon hybridization lines generated by these exponential phonon displacement operators.

Within the dressed NCA approximation for the self energy, we consider only the dressed phonon lines appearing along the noncrossing fermionic hybridization lines, as illustrated in Fig. 4. With this assumption, the effect of the electron-phonon interaction is simply to reweigh each fermionic hybridization line with a phonon-dependent factor, such that the NCA self energy takes the form

$$\begin{aligned}\tilde{\Sigma}_{\alpha\alpha}^\ell(t_1 - t_2) &= w(t_1 - t_2) \\ &\times \sum_{\beta} \Delta_{\alpha\alpha}^\beta(t_1 - t_2) G_{\beta\beta}^{(0)}(t_1 - t_2).\end{aligned}\quad (33)$$

The phonon weight $w(t_1 - t_2)$ is given by

$$\begin{aligned}w(t) &= \exp \left\{ - \sum_q \left(\frac{\lambda_q}{\omega_q} \right)^2 \times \right. \\ &\quad \left. [(1 - \cos \omega_q t) \coth(\beta \omega_q / 2) + i \sin \omega_q t] \right\}.\end{aligned}\quad (34)$$

In terms of the bath spectral density $J(\omega)$, this can be written as

$$w(t) = \exp \{ -Q_2(t) - iQ_1(t) \}, \quad (35)$$

where

$$Q_1(t) = \frac{2}{\pi} \int d\omega \frac{J(\omega)}{\omega} \sin \omega t, \quad (36)$$

$$Q_2(t) = \frac{2}{\pi} \int d\omega \frac{J(\omega)}{\omega} (1 - \cos \omega t) \coth(\beta \omega / 2). \quad (37)$$

The dressed NCA self energy includes many phonon interactions not included in the bare NCA. The self energy diagrams composed of the transformed dot opera-

tors \tilde{d}_σ and \tilde{d}_σ^\dagger can be expanded in terms of the bare dot operators and effectively contain all the hybridization diagram within the wiggly double lines. Also, the polaron shift of U and ϵ is explicitly included within the dressed NCA, but not the bare NCA. One might expect it to be a more appropriate approximation in the polaron limit. On the other hand, it also misses some contributions that are included in the bare NCA (see Fig. 4 (b)) and over-emphasizes others, and at weak coupling to the phonons it might be expected to be less accurate. The two approximations are therefore somewhat complementary, if in a non-rigorous sense; it is reasonable to assume that conclusions supported by both may be robust to the nature of the approximations, while conclusions supported by only one are suspect and should be investigated further.

C. NCA for asymmetric model

We now briefly discuss the structure of the non-crossing approximation for the case of an asymmetric Anderson-Holstein model in which the counter term is not included (i.e. $\delta = 0$ in Eq. (4)). The phonon can then only be created or destroyed in the single electron state or the doubly occupied state, not in the empty state. Such a model might be considered a more physically realistic description of a quantum junction, where one is interested in vibrational states coupled to electrons.

In the bare NCA calculation, the phonon coupling lines only connect points with occupied electron states. The interaction diagrams for the bare NCA self energy therefore no longer have the symmetric structure of Fig. (4), but rather include a different number of phonon inclusions for each of the matrix elements. This is illustrated in Fig. (5).

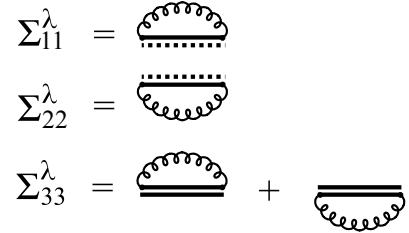


Figure 5. The phonon interaction diagrams for asymmetrical model.

For the dressed NCA, the same Lang-Firsov transformation is performed to eliminate the explicit electron-phonon coupling. The dressed coupling Hamiltonian then remains the same as in the symmetric case. However, the renormalized energy becomes

$$\tilde{\epsilon} = \epsilon - \frac{\lambda^2}{\omega_0}, \quad (38)$$

while the renormalized interaction remains the same as

Eq. (30).

With this coupling, $\epsilon = 0$ does not correspond to a particle-hole symmetric point. In the absence of dot-lead coupling, the charge transfer bands are centered around $\omega_+ = \frac{U}{2} + \frac{\lambda^2}{\omega_0}$ and $\omega_- = -\frac{U}{2} + 3\frac{\lambda^2}{\omega_0}$.

IV. RESULTS

We now discuss the application of the two NCA approaches described above to the Anderson-Holstein impurity model, focusing on a case where the dot has degenerate spin levels ($\epsilon_\uparrow = \epsilon_\downarrow = \epsilon_d$) and obeys particle-hole symmetry ($\epsilon_d = -\frac{U}{2}$) in the absence of phonons. The leads are assumed to be flat with a soft cutoff: $\Gamma_\ell(\omega) = \frac{\Gamma_\ell}{(1+e^{\nu(\omega-\Omega_c)})(1+e^{-\nu(\omega+\Omega_c)})}$, where $\Omega_c = 10$ and $\nu = 10$. We consider only symmetrical couplings to the left and right leads, $\Gamma_L = \Gamma_R = 0.5\Gamma$, and apply the bias voltage V symmetrically such that the chemical potentials are given by $\mu_L = -\mu_R = 0.5V$.

The methods we have described are suitable for the exploration of systems containing multiple electron and phonon baths with complicated densities of states, but we focus on a phonon bath with single mode, $H_b = \omega_0 b^\dagger b$. The electron-phonon coupling Hamiltonian becomes $V_b = \lambda(b^\dagger + b)(n_d - \delta)$ and the strength is characterized by the parameter λ . We assume that all baths are initially at the same inverse temperature $\beta = 10/\Gamma$.

To calculate the spectral function $A(\omega)$ by the double probe scheme, we attach a pair of auxiliary leads to the system and measure the corresponding auxiliary currents. The spectral density of the auxiliary leads is a Gaussian delta function $\Gamma_a(\omega, \omega') = \frac{\eta}{\delta_a \sqrt{\pi}} e^{-[(\omega-\omega')/\delta_a]^2}$ where $\eta = 10^{-4}\Gamma$ and $\delta_a = 10^{-2}\Gamma$. The dot is assumed to be initially empty, and the coupling to the thermally equilibrated leads and phonon bath is turned on at time $t = 0$. The auxiliary spectral function exhibits some transient behavior, and approaches the physical steady state spectral function at sufficiently long time, as discussed in Ref. 79.

A. Symmetric Model

We first consider the system which includes the counter term, $\delta = 1$. For this case, the electron-phonon coupling does not break particle-hole symmetry and the spectral function remains symmetric.

1. Transient dynamics

The left panels of Fig. 6 and Fig. 7 show the transient evolution of the spectral function $A(\omega; t)$. The corresponding right panels display single frequency cuts through this data, highlighting the time evolution of the central peak ($\omega = 0$) and the charge transfer (CT) peak

($\omega/U = 0.5$). We observe an overshooting of the spectral function at short time due to the instantaneous coupling between the dot and the leads. The bare NCA results (Fig. 6) exhibit oscillatory behavior in the amplitude of the central peak. We observe that this is composed of a slower oscillation with a period of $2\pi/\omega_0$, which is associated with the phonon frequency; and a rapid oscillation with a period of $2\pi/U$, which comes from the static energetics of the system. However, in the dressed NCA results (Fig. 7), oscillatory behavior consistent with the phonon frequency is not apparent. The oscillatory behavior predicted by the bare NCA is consistent with predictions made for the Anderson-Holstein model in the spinless $U = 0$ ⁵⁷ and $U = \infty$ cases,⁶⁹ where the local density of states at $\omega = 0$ approaches the steady state in an oscillating manner with the periodicity of the phonon mode. Here, the time-evolution of the entire frequency dependent auxiliary spectral function additionally reveals the transient effect of electron-phonon coupling on the charge transfer peaks.

At long times, the bare NCA exhibits a strong suppression of the CT peaks when the phonon frequency is small. However, this suppression of the CT peaks is not nearly as evident in the dressed NCA results. Conversely, the dressed NCA shows a strong enhancement of the central peak at low phonon frequencies, which is not present in the bare NCA results.

2. Equilibrium steady state spectral function

We next explore the equilibrium spectral function $A(\omega)$ of the system in the limit of long times, where the system has reached its steady or equilibrium state. We consider two types of cuts through the parameter space: the first is the dependence on the phonon frequency ω_0 at constant dot-phonon coupling strength λ , and the second is the λ dependence at constant ω_0 . Here, too, the bare and dressed NCA predict qualitatively different behaviors.

In Fig. 8, $A(\omega)$ is shown for a range of phonon frequencies at intermediate electron-phonon coupling $\lambda = 1.5$. Within bare NCA, shown in panel (a), a set of features at $\omega = \pm n\omega_0$ with $n \in \{1, 2, 3\}$ is visible at low frequencies. These features, corresponding to Kondo replicas or sidebands^{25,32-34,36,77}, appear as a sequence of positive peaks at $\omega = \pm(2n+1)\omega_0$ and negative peaks at $\omega = \pm 2n\omega_0$, and are related to interference effects. In the literature, the Anderson-Holstein impurity model is mostly assumed to be spinless ($U = 0$), and one observes multiple positive side bands due to a resonance with the phonon. For a generic Anderson-Holstein model, negative peaks have previously been predicted in the $T \sim 0$ regime by perturbation theory, but not are exhibited within numerical renormalization group calculation.^{25,77} However, our calculation shows both positive and negative side peaks exist at a finite temperature for generic Anderson-Holstein model. In the high-frequency regime,

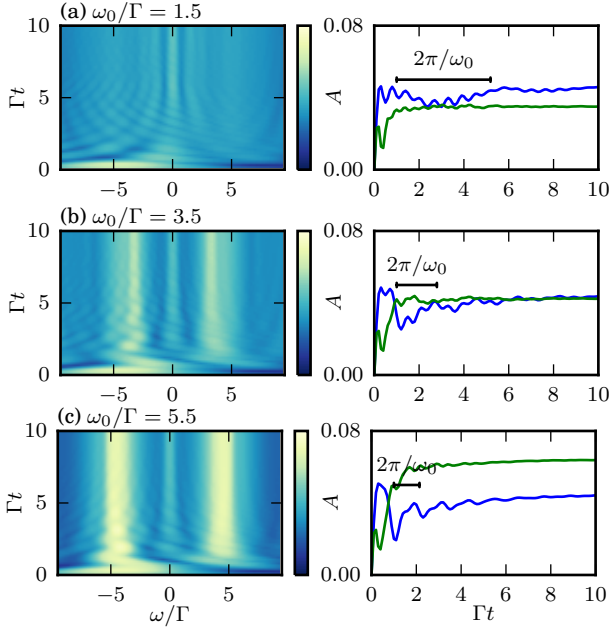


Figure 6. (left panels) The time evolution of the spectral function $A(\omega; t)$ within the **bare NCA** is shown for different phonon frequencies. (right panels) Time dependence of cuts at $\omega = 0$ (blue) and $\omega = U/2$ (green). The time scale $2\pi/\omega_0$ related to the phonon frequency is also plotted for comparison. A symmetric dot with $U = -2\epsilon = 10\Gamma$ is considered at equilibrium $V = 0$. The phonon coupling is set to $\lambda = 1.5\Gamma$ and the counter term is symmetric ($\delta = 1$). The inverse temperature of all baths is $\beta = 10/\Gamma$.

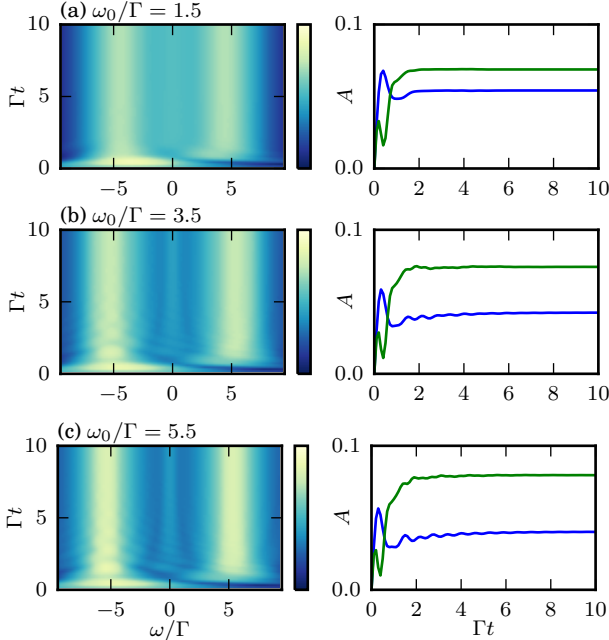


Figure 7. The same as Fig. 6 within the **dressed NCA**. A symmetric dot with $U = -2\epsilon = 10\Gamma$ is considered at equilibrium $V = 0$. The phonon coupling is symmetric with $\lambda = 1.5\Gamma$ and the inverse temperature of all baths is $\beta = 10/\Gamma$.

the Kondo replicas die out and the CT peaks appear. The CT peaks are suppressed by coupling to a low frequency phonon mode, which implies that phonon-induced tunneling dominates the single particle excitation spectrum in this regime.

Replica-like features can also be observed at $\omega = \pm\omega_0$ in the dressed NCA, which is plotted in Fig. 8 (b). However, these side peaks are substantially weaker than those observed in the bare NCA calculation. In the dressed NCA the CT peaks are shifted by the reorganization energy, such that their central frequencies are located at $\omega_{\pm} = \pm \left(\epsilon + \frac{\lambda^2}{\omega_0} \right)$ (as illustrated by the dashed line). A significant enhancement in $A(\omega)$ occurs when the two renormalized CT peaks cross each other. In the low frequency regime $\omega_0 \leq \frac{\lambda^2}{|\epsilon|}$, the two CT peaks merge and form a wide central peak which is clearly unrelated to the Kondo effect. The Kondo peak only develops in the high frequency regime, and in general it is strongly suppressed for a wide range of parameters.

The ω_0 dependence of the central peak $A(\omega = 0)$ exhibits consistent behavior for the two flavors of NCA only at high frequencies (Fig. 8 (c)). At low frequencies, both approximations exhibit enhancement of the central peak, but the context and perhaps the mechanism of the enhancement is different between the two cases. In the bare NCA, the amplitude of the Kondo peak is enhanced as ω_0 decreases because the replicas of the Kondo peak merge when the phonon quasi-states become nearly-degenerate as ω_0 decreases. In the dressed NCA, on the other hand, the enhancement is maximal where the two CT peaks merge at $\omega_0^* = \lambda^2/\epsilon$. The contrast with the bare case is even more notable when one considers that in the bare NCA the CT peaks are almost entirely suppressed at low frequencies.

In Fig. 9 we repeat the previous analysis in a different plane of the parameter space, by taking a cut at a constant (low) phonon frequency ω_0 and a range of λ values. In the bare NCA (Fig 9 (a)), the CT peaks are suppressed as λ increases. One can observe a set of ridge-like features developing along with a strong enhancement of the central Kondo peak. In the large λ regime, the developed side peaks shifted linearly with λ with a spacing of approximately ω_0 between peaks in frequency. These features resemble Kondo replicas^{25,32,34,36,77} but a closer inspection reveals behavior more complicated than simply side peaks generated at the phonon frequency $|\omega| = n\omega_0$. A sharp Kondo peak is only apparent before the crossing point of the ridges. It is significantly enhanced at the crossing point, and is either completely suppressed or split beyond this point.

No Kondo replicas are observed within the dressed NCA (Fig. 9 (b)). The CT peaks are again renormalized, and appear centered at $\omega_{\pm} \approx \pm \left(\epsilon + \frac{\lambda^2}{\omega_0} \right)$ as illustrated by the dashed lines. The crossing at $\lambda^* = \sqrt{\epsilon\omega_0}$ leads to

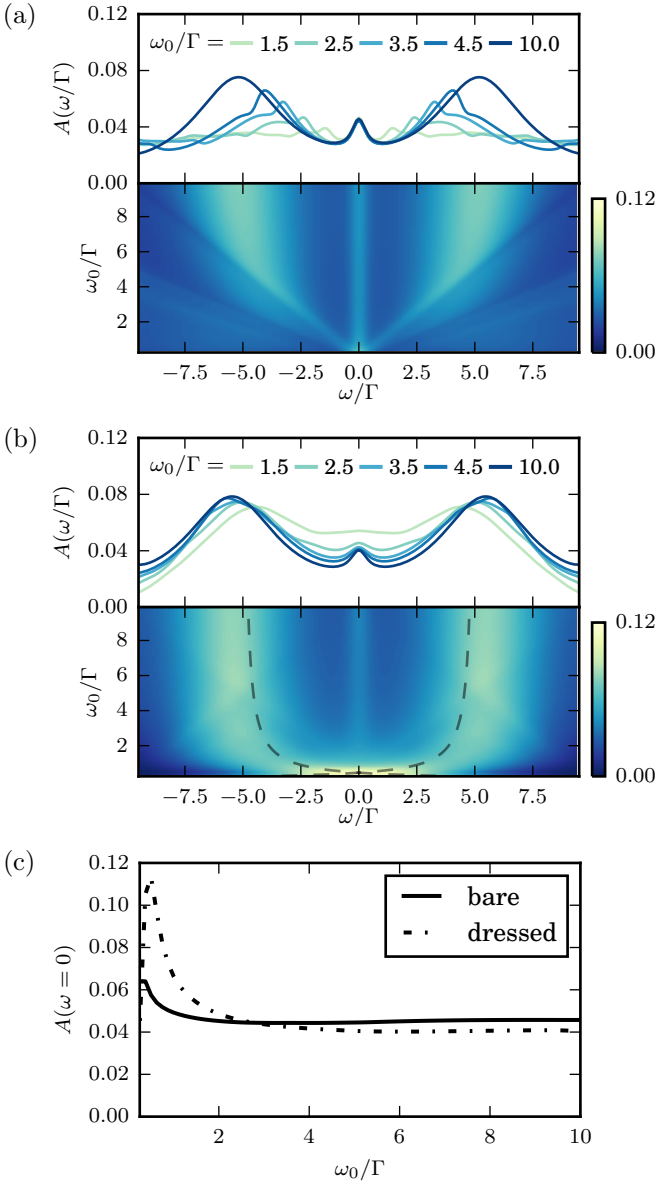


Figure 8. The ω_0 dependence of the spectral function $A(\omega)$ is calculated by (a) **bare NCA** and (b) **dressed NCA** for a symmetric dot at equilibrium $V = 0$ with $U = -2\epsilon = 10\Gamma$. The phonon coupling is $\lambda = 1.5\Gamma$ and the counter term is symmetric ($\delta = 1$). All baths at the same inverse temperature $\beta = 10/\Gamma$. The dashed lines indicate the renormalized charge transfer peak at $\omega_{\pm} = \pm(\epsilon + \frac{\lambda^2}{\omega_0})$. The ω_0 -dependence of the central peak at $\omega = 0$ is plotted in (c).

a strong enhancement near $\omega = 0$. The Kondo peak is only observable for $\lambda < \lambda^*$, and is widened beyond the point where it can be distinguished from the CT bands before the crossing point is reached. This widening effect is not observed in the bare NCA. Past the crossing point, no central feature is visible, in agreement with the bare NCA.

While the striking non-monotonic enhancement of the

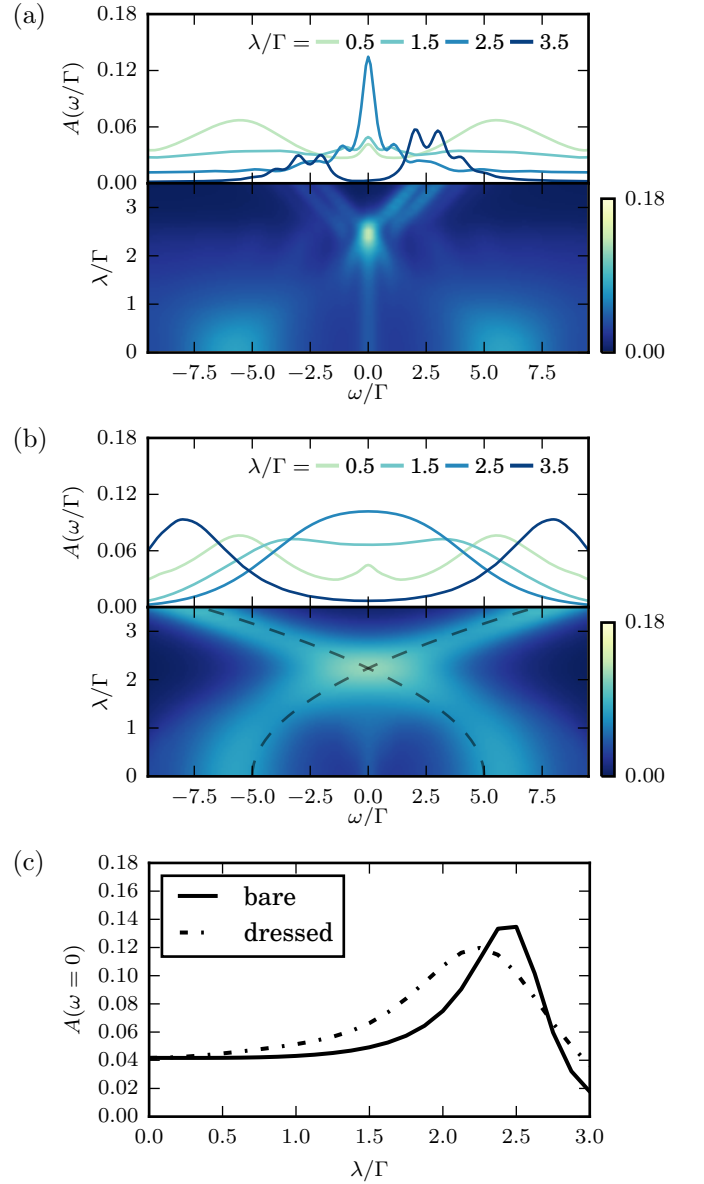


Figure 9. The λ dependence of the spectral function $A(\omega)$ as calculated within the (a) **bare NCA** and (b) **dressed NCA** for a symmetric dot with $U = -2\epsilon = 10\Gamma$ at equilibrium $V = 0$. The phonon coupling is $\omega_0 = 1.0\Gamma$ and the counter term is symmetric ($\delta = 1$). All baths at the same inverse temperature $\beta = 10/\Gamma$. The dashed lines indicate the renormalized charge transfer peak at $\omega_{\pm} = \pm(\epsilon + \frac{\lambda^2}{\omega_0})$. The λ -dependence of the central peak at $\omega = 0$ is plotted in (c).

$\omega = 0$ spectral function is predicted by both approximations, it occurs at a different value of λ in each case (see Fig. 9 (c)). The peak in the dressed NCA occurs precisely at the value of λ for which the effective, dressed \tilde{U} change sign. In this regard, the result is reminiscent of the NRG prediction of Hewson and Meyer,²⁵ where the negative- \tilde{U} Anderson-Holstein model flows to the $U = 0$ behavior. Within the bare NCA, the peak value of $A(\omega = 0)$ occurs

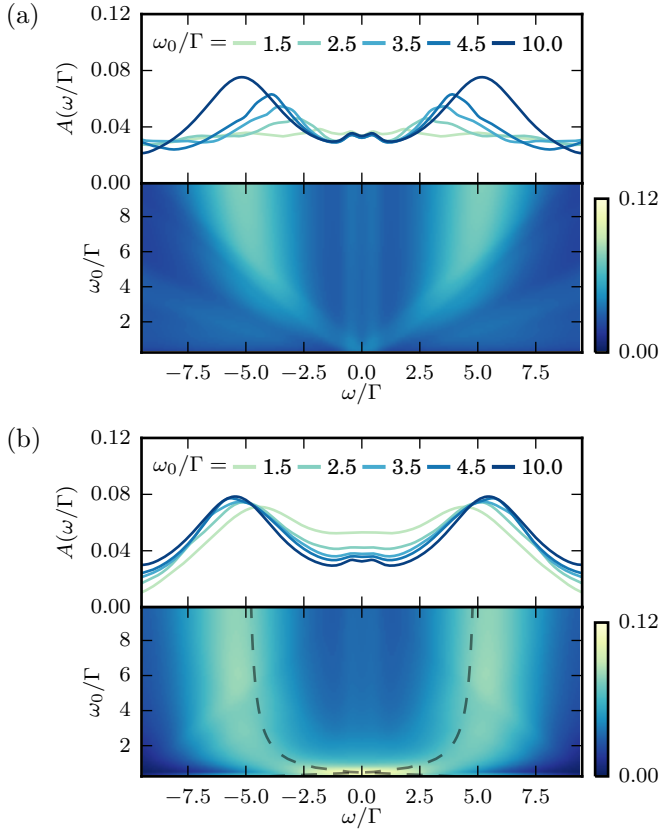


Figure 10. The ω_0 -dependence of the spectral function $A(\omega)$ for a symmetric dot with $U = -2\epsilon = 10\Gamma$ under a nonequilibrium symmetrically applied bias voltage $V = 2\Gamma$ within the (a) **bare NCA** and (b) **dressed NCA**. The phonon coupling is $\lambda = 1.5\Gamma$ and the counter term is symmetric ($\delta = 1$). All baths at the same inverse temperature $\beta = 10/\Gamma$.

for a slightly larger value of λ . Here, the self-consistency of the perturbation theory presumably captures, in an approximate manner, the terms leading to negative- \tilde{U} behavior as well. Lastly, it should be mentioned that this non-monotonic behavior is consistent with the prediction of Ref. 26. We return to this point later in the manuscript.

3. Nonequilibrium steady state spectral function

We now consider a nonequilibrium system driven by a bias voltage $V = 2\Gamma$. The ω_0 dependence of $A(\omega)$ is plotted in Fig. 10. The voltage splitting of Kondo peak^{93,99} can be observed in both approximations. The central Kondo peak splits into two peaks at $\omega = \pm V/2$ independently of the phonon frequency. Kondo replicas are not clearly distinguishable, since the splitting smears out the associated features. However, a set of linearly dependent signatures remains visible.

B. Asymmetric Model

In the following subsection, we consider an Anderson–Holstein model without a counter term, i.e. $\delta = 0$ in Eq. (4). While the isolated dot Hamiltonian is still assumed to remain particle-hole symmetric, the electron–phonon coupling breaks the particle-hole symmetry of the system and results in an asymmetric spectral function. The two NCA formulations we employ take this asymmetry into account in different ways, as pointed out in sec. III C. In addition to the spectral function, we study the effects of the symmetry breaking on transport properties. This is of particular interest, because under a symmetrically applied bias the differential conductance is a symmetric function of frequency even without particle–hole symmetry. Additionally, one may not be able to observe the replicas directly in a transport experiment, due to the nonequilibrium shifting or suppression of the Kondo peak, which would also affect the replicas. We show that an indirect experimental signal of the replica effect may remain.

1. Transient dynamics

Within the bare NCA, the CT peaks and Kondo peak oscillate at the phonon frequency ω_0 , but the oscillations are manifested in different ways (Fig. 11, left panels). In particular, the CT peaks oscillate in *frequency*, while the Kondo peak oscillates in *amplitude*. At short times and in the adiabatic limit, the CT peak oscillations can be explained by oscillating energy levels ($\tilde{\epsilon}_\sigma = \epsilon_\sigma + \frac{2\lambda}{\omega_0} \sin(\omega_0 t + \phi_0)$) with some unknown initial phase. This is illustrated by the black dashed lines in the left panels of Fig. 11. All these features are washed out in the dressed NCA.

2. Steady state spectral function

To explore the effects of phonons on the equilibrium spectral function, we once again plot first the ω_0 dependence at constant λ , and then the λ dependence at constant ω_0 . Within the bare NCA, the Kondo replica features can clearly be seen in Fig. 13 (a), but harder to distinguish in the cuts. They are mixed with a variety of other effect including the low-frequency smearing of the Kondo resonance and the suppression of the positive CT peak. The replica effect and the above-mentioned CT suppression are both stronger at positive frequencies. At small phonon frequencies, the Kondo resonance merges with the negative CT peak.

At the intermediate phonon frequency $\omega_0 = |\epsilon_\sigma - U|$ where the replicas are aligned with the CT peaks, a non-monotonic enhancement of the central peak is evident, and is especially strong at large λ . This can be seen more clearly in the cut shown in Fig. 15 (c). We believe

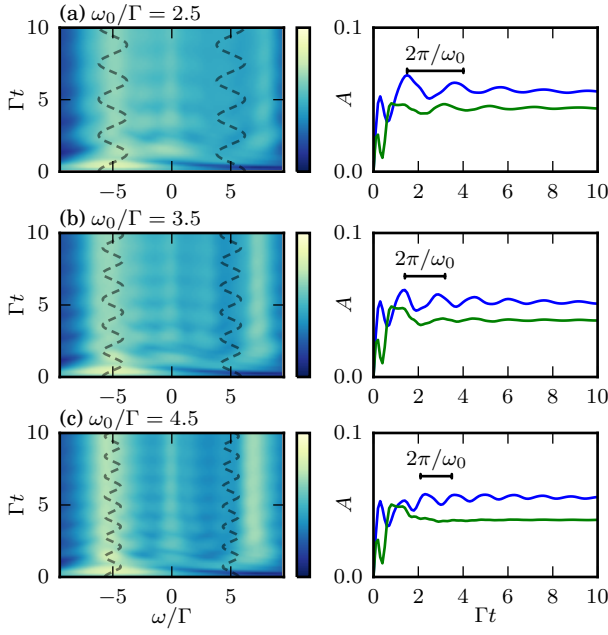


Figure 11. (left panels) The time evolution of the spectral function $A(\omega; t)$ within the **bare NCA** is shown for different phonon frequencies. The frequency oscillations of the CT peaks along with an illustration of the expected energy oscillations in the adiabatic limit (dash lines) are also exhibited. (right panels) Time dependence of cuts at $\omega = 0$ (blue) and $\omega = U/2$ (green). The time scale $2\pi/\omega_0$ related to the phonon frequency is also plotted for comparison. The dot is symmetric with $U = -2\epsilon = 10\Gamma$ at equilibrium $V = 0$. The phonon coupling is $\lambda = 1.5\Gamma$ and the counter term is asymmetric ($\delta = 0$). The inverse temperature of all baths is $\beta = 10/\Gamma$.

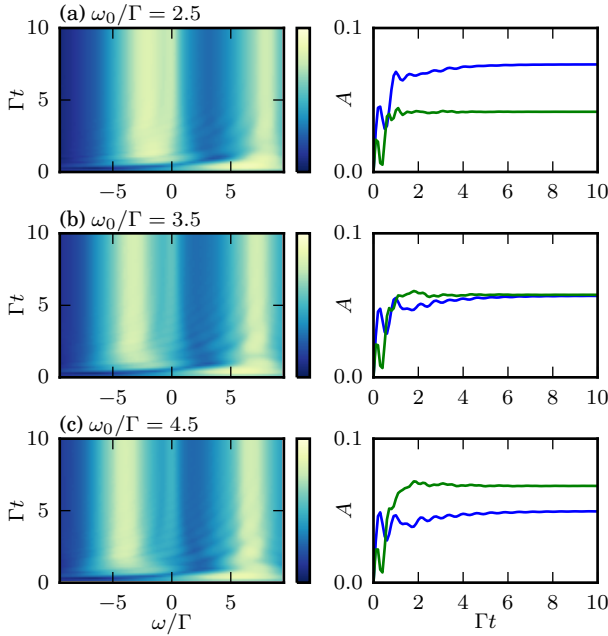


Figure 12. The same as Fig. 11 within the **dressed NCA**. The dot is symmetric with $U = -2\epsilon = 10\Gamma$ at equilibrium $V = 0$. The phonon coupling is asymmetric ($\delta = 0$) with $\lambda = 1.5\Gamma$ and the inverse temperature is $\beta = 10/\Gamma$.

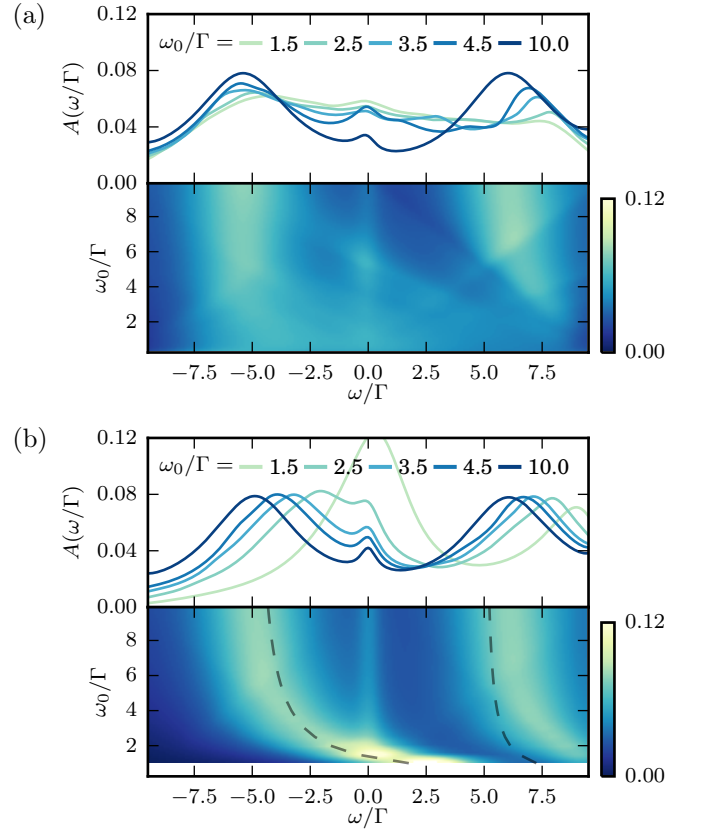


Figure 13. The ω_0 -dependence of the spectral function $A(\omega)$ for a dot in equilibrium as calculated within the (a) **bare NCA** and (b) **dressed NCA**. The electron-phonon coupling is asymmetric ($\delta = 0$) and the coupling strength is $\lambda = 1.5\Gamma$. The dot is symmetric with $U = -2\epsilon = 10\Gamma$. All baths at the same inverse temperature $\beta = 10/\Gamma$.

this is due to a phonon-assisted process which is similar to the Kondo spin-flip process, and which becomes possible for electrons with energies closed to the chemical potential.^{26,100} The effects described here are largely washed out in the dressed NCA.

We continue to investigate the λ dependence at constant ω_0 . Here, we plot the results for both approximations at a relatively large ω_0 (Fig. 14). The bare NCA (panel (a)) shows a suppression of the charge transfer bands and a widening of the Kondo peak. The dressed NCA (panel (b)) shows an asymmetric shift of the CT peaks to approximately $\omega_+ = \frac{U}{2} + \frac{\lambda^2}{\omega_0}$ and $\omega_- = -\frac{U}{2} + 3\frac{\lambda^2}{\omega_0}$, as might be expected in the anti-adiabatic limit. Some deviation from this occurs, especially for the positive CT band. More interestingly, as the CT peak merges with the Kondo peak at $\lambda = \sqrt{\frac{U\omega_0}{6}}$, a strong enhancement occurs. This enhancement is not observed in the bare NCA.

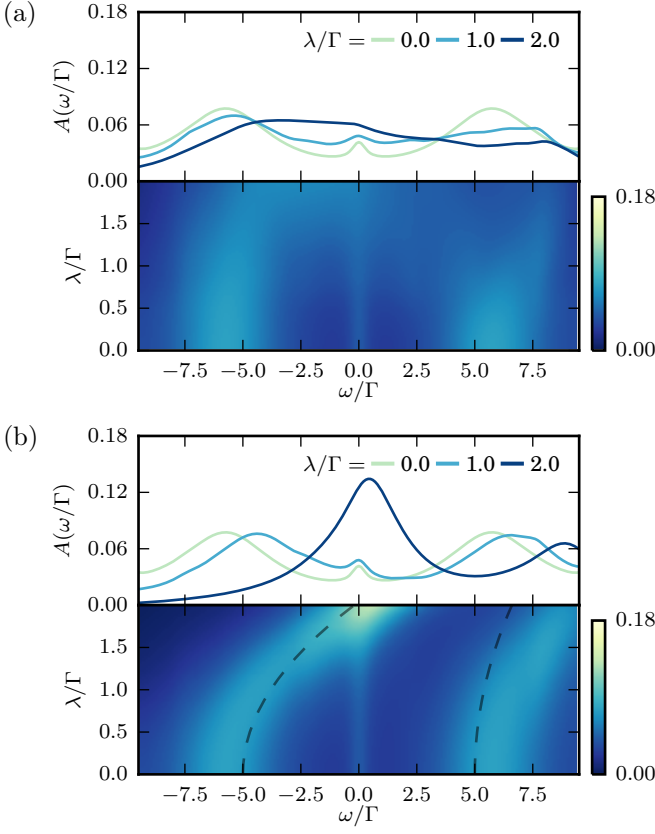


Figure 14. The λ -dependence of the spectral function $A(\omega)$ as calculated within the (a) **bare NCA** and the (b) **dressed NCA** for an equilibrium symmetric dot with $U = -2\epsilon = 10\Gamma$. The phonon frequency is $\omega_0/\Gamma = 2.5$. The dashed lines indicate the center of the CT peaks as estimated by the energy renormalization at the anti-adiabatic limit $\omega_{CT}^+/\Gamma = -\epsilon + \frac{\lambda^2}{\omega_0}$ and $\omega_{CT}^-/\Gamma = \epsilon + 3\frac{\lambda^2}{\omega_0}$. All baths at the same inverse temperature $\beta = 10/\Gamma$.

3. Steady state conductance

Despite the symmetry breaking of the spectral function, the differential conductance $G(V) \equiv \frac{dI}{dV}(V)$ under a symmetrically applied bias ($\mu_L = -\mu_R = V/2$) remains a symmetric function of frequency even without the counter term. The replica effect and the non-monotonic enhancement, as visible in, *e.g.*, Fig. 13, appears in the spectral function, which could in principle be accessible in spectroscopic experiments. However, spectroscopic studies of single molecules in junctions and mesoscopic quantum dots are difficult to perform, and transport experiments are far more common. It is interesting to consider whether these effects are observable in the differential conductance as well as the spectral function; outside of linear response these quantities may differ qualitatively.⁹³ Fig. 15 shows the differential conductance as it varies under the effect of the phonon frequency ω_0 at two different phonon coupling strengths λ . The non-monotonic enhancement remains clearly visible, while the

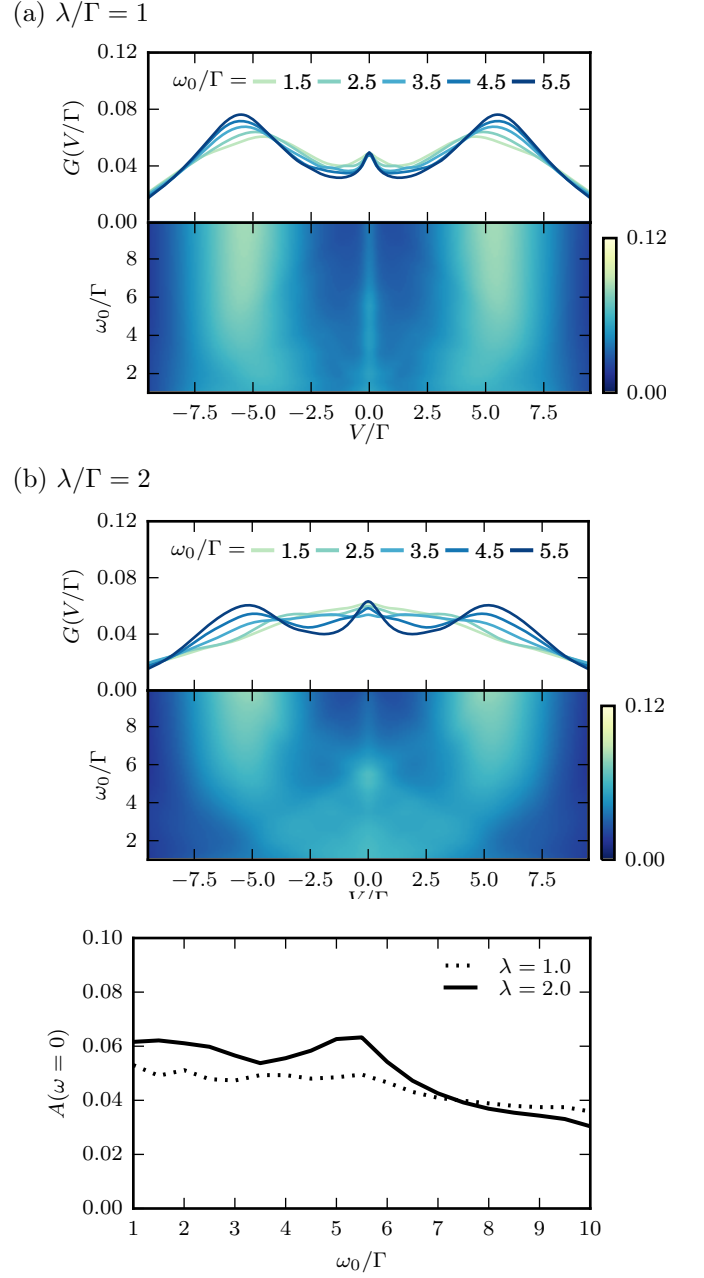


Figure 15. The conductance $G(V)$ as calculated within the **bare NCA** for different electron-phonon coupling (a) $\lambda/\Gamma = 1$ and (b) $\lambda/\Gamma = 2$ with a symmetrically applied bias $\mu_L = \mu_R = V$. The dot is also symmetric with $U = -2\epsilon = 10\Gamma$. Panel (c) shows the ω_0 -dependence of the central peak at $\omega = 0$. All baths at the same inverse temperature $\beta = 10/\Gamma$.

side peaks are substantially weaker than their counterparts in the spectral function. The bare NCA therefore predicts that the non-monotonicity could be observed in transport experiments. Since it is related to the side bands merging with the charge transfer bands, an experimental observation of it could also be considered an indirect confirmation of the replica effect. We note that the dressed NCA also predicts a non-monotonicity, but

one which does not appear related to the replica effect. It will take a more sophisticated theoretical treatment to determine whether this effect is real or an artifact of the two NCA approaches, and to understand more deeply the mechanism that lies behind it.

In Ref. 26, a non-monotonic effective Kondo temperature and zero-bias conductance has been predicted in the Anderson–Holstein model via the consideration of two limiting cases. In particular, for weak electron–phonon coupling $2\lambda^2/\omega_0 \ll U$, the low-energy excitations of the Anderson–Holstein model can be approximated by an isotropic Kondo Hamiltonian with the coupling to phonons leading to an increase in the effective Kondo temperature. On the other hand, for strong electron–phonon coupling $2\lambda^2/\omega_0 \gg U$, the low-energy excitations can be approximated by an anisotropic Kondo Hamiltonian in which the effective Kondo temperature decreases with increasing λ . This crossover behavior is observed in both NCAs, though the implied maximum in the spectral function occurs at a different λ (see also Fig. 9c). Interestingly, when examining the spectral function at all energies simultaneously, a set of higher energy features which appear to be shifted replicas of the maximum is also revealed.

V. CONCLUSIONS

In this paper we formulate and compare two distinct non-crossing approximations for the study of the Anderson–Holstein model. The first approximation, which we call the bare NCA, is a self-consistent resummation based on a self energy which contains the electron–phonon coupling and hybridization with the leads to lowest order. Within the second approximation, which we term the dressed NCA, a Lang–Firsov transformation is first applied, and the resulting transformed set of interactions are then included in a self-consistent, lowest order self energy. We focus on the predictions of both approximations with regard to transient dynamics as well as the non-equilibrium steady state behavior of the spectral function. In general, it should be expected that any flavor of NCA will be inaccurate for low-frequency properties. For example, NCA predicts a broadened and suppressed Kondo resonance when compared with exact numerics.⁷⁹ Due to the paucity of exact and global information related to the dynamical properties of the model, a detailed assessment of the success and failure of the respective methods is not possible even for higher frequency features. On the other hand, we believe it is plausible to favor the bare NCA when the electron–phonon coupling is weak, the dressed NCA when it is strong, and both approaches when they produce consistent results in the intermediate coupling regime. Since the two approximations are based on disparate limits of the electron–phonon portion of the problem, we focus on the intermediate coupling regime in an attempt to assess the validity of the two approximations.

We find that several features appear to be robust within both flavors of NCA. First, the Kondo peak is enhanced in particular regimes, but is universally suppressed in the large electron–phonon coupling regime. Second, low energy tunneling occurs and charge transfer peaks are suppressed when phonon frequency is small compared to other relevant energy scales. Lastly, the voltage splitting of the Kondo peak robustly occurs in the non-equilibrium regime. We expect these features to be real and experimentally reproducible behaviors in the Anderson–Holstein model.

Conversely, several striking dynamical properties appear only within one type of NCA approximation. In particular, the oscillatory transient behavior exhibited in Fig. 11 and the replication of the Kondo peak is only observed within the bare NCA, while polaronic shifts of the charge transfer peaks occur only in the dressed NCA approximation. It is important to note that these observations do not necessarily imply that such behaviors are artifacts. In particular, since the bare NCA is expected to capture accurately the weak electron–phonon situation, it is plausible that the features revealed in Fig. 9 and 11 are real properties of the model in this regime. The dressed NCA may not predict this behavior due to the fact that several low order diagrams associated with the interplay between hybridization and electron–phonon coupling are absent. On the other hand, polaronic effects may only be captured within the dressed NCA, and thus strong coupling shifts of the charge transfer peaks should be expected once the coupling to phonons is sizable.

Perhaps the most important aspect of the work presented here is that it lays the foundation for exact real-time QMC approaches based on expansion around the NCA approximation. These “bold-line” approaches have been successful in the treatment of the simpler Anderson model, and have enabled the simulation of relatively long real time information before the dynamical sign problem becomes problematic. Convergence of these approaches depends crucially on having a reasonably accurate partial summation of diagrams from the outset. With respect to the work presented here, we expect that the bare and dressed NCA approximations should provide a good starting point in the weak and strong electron–phonon coupling regimes, respectively. In addition to validating or falsifying the predictions made by the individual NCA approximations of this paper, real-time QMC approaches that make use of the bare and dressed NCA techniques should allow for the exact simulation of the Anderson–Holstein model in regimes that are currently inaccessible.

ACKNOWLEDGMENTS

We would like to thank Philipp Werner and Andrés Montoya-Castillo for helpful comments and discussions. DRR acknowledges support from NSF CHE-146802. AJM acknowledges support from NSF DMR-1308236.

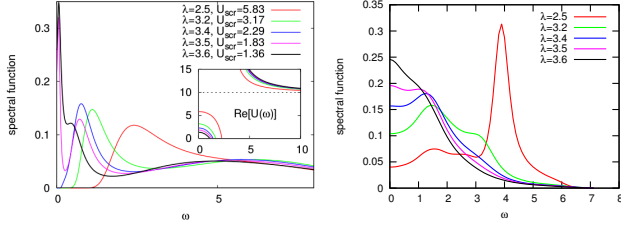


Figure 16. Left: Evolution of the spectral function across the metal–insulator transition (gap closing) by increasing the phonon coupling. Right: The spectral function $A(\omega)$ in the **strong** coupling regime is calculated within the dressed NCA for a symmetric dot with $U = -2\epsilon = 10\Gamma$ at equilibrium $V = 0$. The density of state is of the semi-circular form $\Gamma(\omega) = \sqrt{4t^2 - \omega^2}$ with $t = 1$. The phonon coupling is $\omega_0 = 3.0\Gamma$ and the counter term is symmetric ($\delta = 1$). The baths are maintained at a temperature $\beta\Gamma = 50$.

Appendix A: Comparison with DMFT-based Monte Carlo results

The top panel of Fig. 3 of Ref. 98 illustrates the behavior of the spectral function of an Anderson–Holstein problem computed via analytical continuation of *exact* imaginary-time quantum Monte Carlo as a function of increasing electron–phonon coupling, and is analogous to

our Fig. 9. While it is difficult to make a direct comparison between these results and the results presented in our work due to the fact that the previous results were obtained self-consistently in the context of dynamical mean field theory, we have computed the spectral function for the same model and parameters within the NCA approaches outlined in this paper. In this sense, the results of Fig. 16 represent a type of non-iterated NCA impurity solution in the DMFT context. The electron–phonon coupling parameters used in Fig. 3 of Ref. 98 are sufficiently large to render the bare NCA unstable. On the other hand, the dressed NCA is in qualitative agreement with the analytically continued results.

Quantitatively, the dressed NCA produces peaks in positions similar to those obtained by Monte Carlo for large λ , but the $\omega = 0$ and low frequency peaks are broadened and suppressed when compared to those of the analytically continued exact data. This broadening and suppression appears to be a general feature of NCA.⁷⁹ While the behavior of the gap closing feature can be observed in both the NCA and the analytically continued Monte Carlo data, it is still unclear to what degree the differences in the spectral functions are due to the effects of analytical continuation and the self-consistency of the DMFT calculation.

- ¹ N. W. Ashcroft and N. D. Mermin, *Solid State Physics* (Saunders College, 1976).
- ² S. V. Aradhya and L. Venkataraman, *Nat. Nanotechnol.* **8**, 399 (2013).
- ³ A. Nitzan and M. A. Ratner, *Science* **300**, 1384 (2003).
- ⁴ X. H. Qiu, G. V. Nazin, and W. Ho, *Science* **299**, 542 (2003).
- ⁵ C. Joachim and M. A. Ratner, *Proc. Natl. Acad. Sci. U. S. A.* **102**, 8801 (2005).
- ⁶ Y. C. Chen, M. Zwolak, and M. Di Ventra, *Nano Lett.* **3**, 1691 (2003).
- ⁷ N. Li, J. Ren, L. Wang, G. Zhang, P. Hänggi, and B. Li, *Rev. Mod. Phys.* **84**, 1045 (2012).
- ⁸ Y. Dubi and M. Di Ventra, *Rev. Mod. Phys.* **83**, 131 (2011).
- ⁹ G. D. Scott and D. Natelson, *ACS Nano* **4**, 3560 (2010).
- ¹⁰ N. A. Zimbovskaya and M. R. Pederson, *Phys. Rep.* **509**, 1 (2011).
- ¹¹ L. H. Yu, Z. K. Keane, J. W. Ciszek, L. Cheng, M. P. Stewart, J. M. Tour, and D. Natelson, *Phys. Rev. Lett.* **93**, 266802 (2004).
- ¹² D. Rakhmievitch, R. Korytár, A. Bagrets, F. Evers, and O. Tal, *Phys. Rev. Lett.* **113**, 236603 (2014).
- ¹³ J. Gaudioso, L. J. Lauhon, and W. Ho, *Phys. Rev. Lett.* **85**, 1918 (2000).
- ¹⁴ M. Capone, M. Fabrizio, C. Castellani, and E. Tosatti, *Rev. Mod. Phys.* **81**, 943 (2009).
- ¹⁵ S. Dal Conte, C. Giannetti, G. Coslovich, F. Cilento, D. Bossini, T. Abebaw, F. Banfi, G. Ferrini, H. Eisaki, M. Greven, A. Damascelli, D. van der Marel, and F. Parmigiani, *Science* **335**, 1600 (2012).
- ¹⁶ C. Gadermaier, A. S. Alexandrov, V. V. Kabanov, P. Kusar, T. Mertelj, X. Yao, C. Manzoni, D. Brida, G. Cerullo, and D. Mihailovic, *Phys. Rev. Lett.* **105**, 257001 (2010).
- ¹⁷ C. Gadermaier, V. V. Kabanov, A. S. Alexandrov, L. Stojchevska, T. Mertelj, C. Manzoni, G. Cerullo, N. D. Zhigadlo, J. Karpinski, Y. Q. Cai, X. Yao, Y. Toda, M. Oda, S. Sugai, and D. Mihailovic, *Phys. Rev. X* **4**, 011056 (2014).
- ¹⁸ L. Perfetti, P. A. Loukakos, M. Lisowski, U. Bovensiepen, H. Berger, S. Biermann, P. S. Cornaglia, A. Georges, and M. Wolf, *Phys. Rev. Lett.* **97**, 067402 (2006).
- ¹⁹ L. Perfetti, P. A. Loukakos, M. Lisowski, U. Bovensiepen, M. Wolf, H. Berger, S. Biermann, and A. Georges, *New J. Phys.* **10**, 053019 (2008).
- ²⁰ M. Capone, C. Castellani, and M. Grilli, *Adv. Condens. Matter Phys.* **2010**, 920860 (2010).
- ²¹ D. Fausti, R. I. Tobey, N. Dean, S. Kaiser, A. Dienst, M. C. Hoffmann, S. Pyon, T. Takayama, H. Takagi, and A. Cavalleri, *Science* **331**, 189 (2011).
- ²² S. Kaiser, S. R. Clark, D. Nicoletti, G. Cotugno, R. I. Tobey, N. Dean, S. Lupi, H. Okamoto, T. Hasegawa, D. Jaksch, and A. Cavalleri, *Sci. Rep.* **4**, 3823 (2014).
- ²³ P. W. Anderson, *Phys. Rev.* **124**, 41 (1961).
- ²⁴ T. Holstein, *Ann. Phys. (N. Y.)* **8**, 325 (1959).
- ²⁵ A. Hewson and D. Meyer, *J. Phys. Condens. Matter* **14**, 23 (2001).
- ²⁶ P. S. Cornaglia, H. Ness, and D. R. Grempel, *Phys. Rev. Lett.* **93**, 147201 (2004).

- ²⁷ P. Werner and A. J. Millis, Phys. Rev. Lett. **99**, 146404 (2007).
- ²⁸ J. E. Han, Phys. Rev. B **81**, 113106 (2010).
- ²⁹ A. Georges, G. Kotliar, W. Krauth, and M. J. Rozenberg, Rev. Mod. Phys. **68**, 13 (1996).
- ³⁰ P. Werner and M. Eckstein, Phys. Rev. B **88**, 165108 (2013).
- ³¹ D. Golež, M. Eckstein, and P. Werner, Phys. Rev. B **92**, 195123 (2015).
- ³² J. Paaske and K. Flensberg, Phys. Rev. Lett. **94**, 176801 (2005).
- ³³ A. Jovchev and F. B. Anders, Phys. Rev. B **87**, 195112 (2013).
- ³⁴ R. Seoane Souto, A. L. Yeyati, A. Martín-Rodero, and R. C. Monreal, Phys. Rev. B **89**, 085412 (2014).
- ³⁵ K. F. Albrecht, A. Martín-Rodero, R. C. Monreal, L. Mühlbacher, and A. Levy Yeyati, Phys. Rev. B **87**, 085127 (2013).
- ³⁶ K. F. Albrecht, A. Martín-Rodero, J. Schachenmayer, and L. Mühlbacher, Phys. Rev. B **91**, 064305 (2015).
- ³⁷ A. Mitra, I. Aleiner, and A. J. Millis, Phys. Rev. B **69**, 245302 (2004).
- ³⁸ A. Mitra, I. Aleiner, and A. J. Millis, Phys. Rev. Lett. **94**, 076404 (2005).
- ³⁹ R. Härtle, C. Benesch, and M. Thoss, Phys. Rev. Lett. **102**, 146801 (2009).
- ⁴⁰ M. G. Schultz and F. von Oppen, Phys. Rev. B **80**, 033302 (2009).
- ⁴¹ M. Esposito and M. Galperin, Phys. Rev. B **79**, 205303 (2009).
- ⁴² M. Esposito and M. Galperin, J. Phys. Chem. C **114**, 20362 (2010).
- ⁴³ W. Dou, A. Nitzan, and J. E. Subotnik, J. Chem. Phys. **142**, 084110 (2015).
- ⁴⁴ S. Tikhodeev, M. Nataro, K. Makoshi, T. Mii, and H. Ueba, Surf. Sci. **493**, 63 (2001).
- ⁴⁵ T. Mii, S. Tikhodeev, and H. Ueba, Surf. Sci. **502-503**, 26 (2002).
- ⁴⁶ M. Galperin, M. A. Ratner, and A. Nitzan, J. Chem. Phys. **121**, 11965 (2004).
- ⁴⁷ A. Ueda and M. Eto, Phys. Rev. B **73**, 235353 (2006).
- ⁴⁸ L. K. Dash, H. Ness, and R. W. Godby, J. Chem. Phys. **132**, 104113 (2010).
- ⁴⁹ L. K. Dash, H. Ness, and R. W. Godby, Phys. Rev. B **84**, 085433 (2011).
- ⁵⁰ B. Dong, G. H. Ding, and X. L. Lei, Phys. Rev. B **88**, 075414 (2013).
- ⁵¹ M. Galperin, A. Nitzan, and M. A. Ratner, Phys. Rev. B **73**, 45314 (2006).
- ⁵² M. Galperin, A. Nitzan, and M. A. Ratner, Phys. Rev. B **76**, 035301 (2007).
- ⁵³ R. C. Monreal, F. Flores, and A. Martín-Rodero, Phys. Rev. B **82**, 235412 (2010).
- ⁵⁴ S. Sayyad and M. Eckstein, Phys. Rev. B **91**, 104301 (2015).
- ⁵⁵ A. Martín-Rodero, A. Levy Yeyati, F. Flores, and R. C. Monreal, Phys. Rev. B **78**, 235112 (2008).
- ⁵⁶ L. Mühlbacher and E. Rabani, Phys. Rev. Lett. **100**, 176403 (2008).
- ⁵⁷ J. Klatt, L. Mühlbacher, and A. Komnik, Phys. Rev. B **91**, 155306 (2015).
- ⁵⁸ R. Hützen, S. Weiss, M. Thorwart, and R. Egger, Phys. Rev. B **85**, 121408 (2012).
- ⁵⁹ L. Simine and D. Segal, J. Chem. Phys. **138**, 214111 (2013).
- ⁶⁰ L. Simine and D. Segal, J. Chem. Phys. **141**, 014704 (2014).
- ⁶¹ K. F. Albrecht, H. Wang, L. Mühlbacher, M. Thoss, and A. Komnik, Phys. Rev. B **86**, 081412 (2012).
- ⁶² H. Wang and M. Thoss, J. Phys. Chem. A **117**, 7431 (2013).
- ⁶³ K. F. Albrecht, H. Soller, L. Mühlbacher, and A. Komnik, Phys. E **54**, 15 (2013).
- ⁶⁴ O. Entin-Wohlman, A. Aharony, and Y. Meir, Phys. Rev. B **71**, 035333 (2005).
- ⁶⁵ J. Koch and F. Von Oppen, Phys. Rev. Lett. **94**, 206804 (2005).
- ⁶⁶ J. Koch, M. Semmelhack, F. Von Oppen, and A. Nitzan, Phys. Rev. B **73**, 155306 (2006).
- ⁶⁷ R. C. Monreal and A. Martín-Rodero, Phys. Rev. B **79**, 115140 (2009).
- ⁶⁸ S. Maekawa, J. Ko, G. Scho, J. Martinek, Y. Utsumi, H. Imamura, and J. Barnas, Phys. B **91**, 20 (2003).
- ⁶⁹ A. Goker and B. Uyanik, Phys. Lett. A **376**, 2735 (2012).
- ⁷⁰ P. Roura-Bas, L. Tosi, and A. A. Aligia, Phys. Rev. B **87**, 195136 (2013).
- ⁷¹ R. Härtle and M. Thoss, Phys. Rev. B **83**, 115414 (2011).
- ⁷² E. Y. Wilner, H. Wang, G. Cohen, M. Thoss, and E. Rabani, Phys. Rev. B **88**, 045137 (2013).
- ⁷³ E. Y. Wilner, H. Wang, M. Thoss, and E. Rabani, Phys. Rev. B **89**, 205129 (2014).
- ⁷⁴ P. S. Cornaglia, D. R. Grempel, and H. Ness, Phys. Rev. B **71**, 075320 (2005).
- ⁷⁵ P. S. Cornaglia, G. Usaj, and C. A. Balseiro, Phys. Rev. B **76**, 241403 (2007).
- ⁷⁶ E. Eidelstein, D. Goberman, and A. Schiller, Phys. Rev. B **87**, 075319 (2013).
- ⁷⁷ M. A. Laakso, D. M. Kennes, S. G. Jakobs, and V. Meden, New J. Phys. **16**, 023007 (2014).
- ⁷⁸ L. Arrachea and M. J. Rozenberg, Phys. Rev. B **72**, 41301 (2005).
- ⁷⁹ G. Cohen, D. R. Reichman, A. J. Millis, and E. Gull, Phys. Rev. B **89**, 115139 (2014).
- ⁸⁰ J. König, H. Schoeller, and G. Schön, Phys. Rev. Lett. **76**, 1715 (1996).
- ⁸¹ M. Schiró and M. Fabrizio, Phys. Rev. B **79**, 153302 (2009).
- ⁸² E. Gull, A. J. Millis, A. I. Lichtenstein, A. N. Rubtsov, M. Troyer, and P. Werner, Rev. Mod. Phys. **83**, 349 (2011).
- ⁸³ G. Cohen and E. Rabani, Phys. Rev. B **84**, 075150 (2011).
- ⁸⁴ G. Cohen, E. Y. Wilner, and E. Rabani, New J. Phys. **15**, 073018 (2013).
- ⁸⁵ G. Cohen, E. Gull, D. R. Reichman, A. J. Millis, and E. Rabani, Phys. Rev. B **87**, 195108 (2013).
- ⁸⁶ E. Gull, D. R. Reichman, and A. J. Millis, Phys. Rev. B **82**, 075109 (2010).
- ⁸⁷ N. E. Bickers, Rev. Mod. Phys. **59**, 845 (1987).
- ⁸⁸ T. Pruschke and N. Grewe, Zeitschrift für Phys. B Condens. Matter **74**, 439 (1989).
- ⁸⁹ N. S. Wingreen and Y. Meir, Phys. Rev. B **49**, 40 (1994).
- ⁹⁰ K. Haule, S. Kirchner, J. Kroha, and P. Wölfle, Phys. Rev. B **64**, 155111 (2001).
- ⁹¹ M. Eckstein and P. Werner, Phys. Rev. B **82**, 115115 (2010).
- ⁹² E. Gull, D. R. Reichman, and A. J. Millis, Phys. Rev. B **84**, 085134 (2011).
- ⁹³ G. Cohen, E. Gull, D. R. Reichman, and A. J. Millis,

- Phys. Rev. Lett. **112**, 146802 (2014).
- ⁹⁴ G. Cohen, E. Gull, D. R. Reichman, and A. J. Millis, Phys. Rev. Lett. **115**, 266802 (2015).
- ⁹⁵ A. J. White and M. Galperin, Phys. Chem. Chem. Phys. **14**, 13809 (2012).
- ⁹⁶ E. Lebanon and A. Schiller, Phys. Rev. B **65**, 035308 (2001).
- ⁹⁷ Q. F. Sun and H. Guo, Phys. Rev. B **64**, 153306 (2001).
- ⁹⁸ P. Werner and A. J. Millis, Phys. Rev. Lett. **104**, 146401 (2010).
- ⁹⁹ Y. Meir, N. S. Wingreen, and P. A. Lee, Phys. Rev. Lett. **70**, 2601 (1993).
- ¹⁰⁰ A. Hewson, *The Kondo Problem to Heavy Fermions* (Cambridge University Press, 1993).